# Effects of mechanical-activation and $TiO_2$ addition on the behavior of two-step sintered steatite ceramics

Anja Terzić[a, *]

anja.terzic@institutims.rs

Nina Obradović[b]

Darko Kosanović[b]

Jovica Stojanović[c]

Antonije Đorđević[d, e]

Ljubiša Andrić[c]

Vladimir B. Pavlović[b]

[a]Institute for Material Testing IMS, Vojvode Mišića Bl. ~~43~~43, 11000 ~~Belgrade~~Belgrade, Serbia

[b]Institute of Technical Sciences, Serbian Academy of Sciences and Arts, Knez Mihailova St. ~~35~~35, 11000 ~~Belgrade~~Belgrade, Serbia

[c]Institute for Technology of Nuclear and Other Mineral Raw Materials, Franchet ~~d'Esperey 86~~d'Esperey 86, 11000 ~~Belgrade~~Belgrade, Serbia

[d]School of Electrical Engineering, University of Belgrade, Kralja Aleksandra Bl. ~~73~~73, 11000 ~~Belgrade~~Belgrade, Serbia

[e]Serbian Academy of Sciences and Arts, Knez Mihailova St. ~~35~~35, 11000 ~~Belgrade~~Belgrade, Serbia

*Corresponding author.

**Abstract**

Steatite, as ceramic with composition predominantly resting on magnesium silicate, was produced from economic resources – talc, aluminosilicate clays, and either $BaCO_3$ or feldspar as flux. Titanium dioxide was a doping agent. Four steatite mixtures were mechanically activated in a planetary ball mill for 30, 45 or ~~60~~60 min, prior to the thermal treatment. Two-step sintering with initial phase set at ~~1350 °C~~ 1350 °C and holding period conducted at ~~1250 °C~~ 1250 °C was applied to initiate diffusion and prevent grain growth. Thereby, a high density ceramic material with low-porous submicron structure was acquired. The effects of $TiO_2$ addition on densification, microstructure, and dielectric characteristics of steatites were monitored. The thermal stability of green mixtures was tested by differential thermal and thermogravimetric analyses. Changes in crystallinity and mineral phase composition were observed by the X-ray diffraction technique. Microstructural visualization with spatial arrangements of individual chemical elements on surface of the sintered ceramics was acquired by scanning electron microscopy accompanied with EDS mapping. In order to test the possibility of employment of the obtained steatites in insulation materials, electrical measurements were conducted by recording variations of the dielectric constant and loss tangent as a function of alternations in the mix-design and the mechanical activation period.

**Keywords:** A. Sintering; B. Electron microscopy; B. X-ray methods; B. Microstructure-final; C. Dielectric properties; D. MgO; E. Insulators

# 1 Introduction

Steatite is a ceramic material with composition predominantly resting on magnesium silicate. Due to its accented dielectric properties, steatite is mainly employed in the electrical engineering [1,2]. This ceramic exhibits extreme hardness and favorable electrical properties, as well as adequate refractoriness and low dielectric loss [3,4]. By showing good insulation predispositions, steatite has been used in a number of applications such as: element formers, thermostat casings, regulator bases, parts of switches and plugs, bulb socket bases, heating element holders, etc [5–9]. Due to the good bio-compatibility with human bone structure, this material took over the role of artificial

implants in dentistry and medicine [9–12].

Steatite is appraised as a cost-effective ceramic, especially as it can be used as alumina substitution, due to its facilitated forming and lower sintering temperature (approximately ~~1400 °C~~ 1400 °C depending on the sintering route) [13,14]. As the main goal is to acquire the structural equivalent to that of natural mineral enstatite ($Mg_3(Si_4O_{10})(OH)_2$), steatite ceramic can be produced from entirely economic resources such as talc and plastic aluminosilicate clay [15–17]. The final structure acquired through crystallization, fusion and dissolution of mineral phases incorporates at least 70% crystalline protoenstatite ($MgSiO_3$) and remaining 30% of amorphous phase [18–20]. Vitreous phase surrounds grains and subsequently merges the crystalline 'skeleton' into a solid scarcely porous ceramic material [21,22]. Thereby, the performance of this crystalline ceramic is ruled by ratio of formed crystalline and liquid phases, amount of pores and the presence of heterogeneities [23].

Extremely dense ceramic with sub-micrometric crystalline particles is difficult to obtain via traditional sintering. Of numerous sintering methods specifically targeted at the forming of the dense structures, the two-step sintering is probably the simplest yet highly efficient procedure [24–28]. High temperatures initiate diffusion and unlock the matter transport mechanism which enables structural densification, but also promotes the grain growth. In order to reach the high density and extreme hardness in a ceramic material, it is necessary to create a low-porous submicron structure. During the two-step sintering, a ceramic body is rapidly subjected to a high temperature, only to be subsequently cooled and kept in a 'sintering holding' interval, i.e. the second sintering stage [29]. During the second isothermal stage, the samples are exposed to prolonged heating at a lower temperature. Such sintering route suppresses the grain growth initially accelerated by a high temperature due to the structural freezing [29,30]. Even though crystals are not growing, the structure undergoes densification in a temperature range called the 'kinetic window' [29]. During this period the most of the residual porosity is eliminated. For this procedure, it is important to obtain the critical density (at least 70% of the true density) during the first stage. Thereby a network of grain boundaries anchored by joints in the triple points is created. The joints have higher activation energy for migration than the grain boundaries, which interrupts the grain growth, where as the densification is not affected [30,31].

Despite extensive researches and numerous literature reports on various dielectric ceramic materials [32–39], a very few studies are investigating the possibilities of low-cost steatite production [16,17,21]. In this paper, thermal and dielectric performances of the steatites with mix-design based on economic resources (talc, bentonite, kaolin clay, barium carbonate, feldspar) were investigated. The steatite mixtures were submitted to the two-step sintering procedure with the initial phase set at ~~1350 °C,~~ 1350 °C, and the sintering holding period conducted at ~~1250 °C.~~ 1250 °C. The effects of the addition of titanium dioxide doping agent on the crystallization, sintering route and densification, microstructure, and dielectric characteristics of steatite ceramics were monitored.

# 2 Experimental

Four steatite mixtures were prepared for the experiment. The mix-design is provided in Table 1. Talc was obtained from Bela Stena deposit, Serbia. Bentonite originated from Jelenkovac deposit, Serbia. Kaolin clay is acquired from Crna Dolina deposit, Bosnia and Herzegovina. Feldspar -$KAlSi_3O_8$ (Bujanovac deposit, Serbia) and barium carbonate – $BaCO_3$ (Acros Organics, India) were applied as fluxing agents in order to enable and control the formation of amorphous matter during the sintering. Titanium dioxide – $TiO_2$ (Fisher Chemicals, UK) was used as a doping agent. The samples' abbreviations S1 and S2 where used for talc ~~+ kaolin~~ + kaolin clay ~~+ feldspar~~ + feldspar and talc ~~+ bentonite + BaCO~~ + bentonite + $BaCO_3$ mixtures, respectively. S1T and S2T abbreviations were employed in $TiO_2$ doped mixtures with the same mix design as S1 and S2.

**Table 1** Mix design of steatite ceramic materials.

alt-text: Table 1

| Sample | S1 | S2 | S1T | S2T |
|---|---|---|---|---|
| Raw material | | | | |
| Talc | 80% | 80% | 80% | 80% |
| Bentonite | | 10% | | 9% |
| Kaolin clay | 10% | | 9% | |
| Feldspar | 10% | | 9% | |
| $BaCO_3$ | | 10% | | 9% |
| $TiO_2$ | | | 2% | 2% |

Chemical compositions were analyzed on an ED 2000 XRF spectrophotometer (Oxford Instruments, UK). A representative sample ~~100~~(100 g) of each mixture was pulverized in a laboratory vibratory mill prior to the X-ray fluorescence testing. Loss on ignition (LoI) was determined as a weight difference between ~~20 °~~ 20 ° and ~~1000 °C.~~ 1000 °C. Chemical analyses are presented in Table 2.

**Table 2** Chemical analysis of green steatite mixtures.

alt-text: Table 2

| Oxide, % | S1 | S2 | S1T | S2T |
|---|---|---|---|---|
| $SiO_2$ | 63.2 | 56.9 | 62.4 | 55.8 |
| $K_2O$ | 0.35 | 0.42 | 0.30 | 0.38 |
| $Na_2O$ | 0.48 | 0.40 | 0.42 | 0.37 |
| $Fe_2O_3$ | 0.58 | 0.78 | 0.57 | 0.73 |
| CaO | 0.59 | 0.62 | 0.58 | 0.60 |
| MgO | 22.7 | 28.3 | 22.5 | 27.5 |
| $Al_2O_3$ | 6.70 | 5.3 | 6.60 | 5.0 |
| $TiO_2$ | – | – | 1.03 | 1.75 |
| LoI | 5.40 | 7.28 | 5.60 | 7.90 |

Prior to the sintering, green steatite powders were submitted to the mechano-chemical activation in a high-energy planetary mill with $ZrO_2$ vessels and balls (Pulverisette 5, Fritsch). The ratio between the batch and grinding balls was 1: 40. The milling process was performed in air in the time periods of 30, 45, and ~~60~~60 min. Upon micronization, non-activated and activated S1, S2, S1T and S2T binder-free powders were compacted into cylindrical tablets using the uniaxial double action in an ~~8~~8 mm diameter tool (Hydraulic press RING, P-14, VEB THURINGER; ~~0.3~~0.3 g of powder; ~~2000kg cm~~2000 kg $cm^{-2}$ load). Thus prepared tablets were placed in an alumna boat and submitted to the two-step sintering in a tube furnace (Lenton Thermal Design Type 1600). The non-isothermal sintering regime was applied up to ~~1350~~1350 °C (heating rate ~~20~~20 °C/min, cooling rate ~~10~~10 °C/min), which was followed by dwelling at ~~1250~~1250 °C for ~~4~~4 h. The sintering was conducted in an air atmosphere.

The mineralogical phase composition of the steatite powders upon sintering was determined by X-ray powder diffraction technique. XRD patterns were obtained on a Philips PW-1710 automated diffractometer using a Cu tube. The instrument operates at 40 kV voltage and 30 mA current. It is equipped with a slanted graphite monochromator and a scintillation counter. The intensities of the diffracted CuKα X-ray emission (λ = 1.54178 Å) were measured at the ambient temperature in the intervals 0.02°2$\theta$ in the 2$\theta$ Bragg angle range from 4 do 65°2$\theta$, counting for 0.5 s.

The thermal behavior of the green mixtures was monitored by simultaneous TG-DTA Setsys analyzing system (SETARAM Instrumentation, France) in the temperature range between the ambient temperature and ~~1200~~1200 °C under the air flow of ~~20~~20 ml $min^{-1}$, in an $Al_2O_3$ pan. The experiments were conducted using a heating rate of ~~20~~20 °C $min^{-1}$.

The morphology of the crushed steatite samples obtained after sintering was characterized by scanning electron microscopy (JEOL, JSM-6390 LV) accompanied by energy-dispersive X-ray spectroscopic (EDS) mapping. Parts of the sintered tablets, whose surface was not polished prior to the imaging, were used in the analysis. The samples were covered with an Au film to improve the conductivity during recording. The sizes of the pores and particles in the SEM microphotographs were analyzed and estimated using Gwyddion software for the image analysis.

The relative dielectric permittivity (dielectric constant) and the loss tangent of the sintered samples were measured using an Agilent E5061A network analyzer, in the frequency range between ~~1~~1 MHz and ~~500~~500 MHz. The samples were placed in a coaxial test chamber. The reflection coefficient of the chamber was measured by the analyzer and the relative complex permittivity of the samples was extracted using an electrostatic model.

# 3 Results and discussion

The changes in the mineral phase composition induced by the two-step sintering of the steatite mixes with respect to the variations in the mix-design, the applied mechano-chemical activation pretreatment and the employment of $TiO_2$ doping agent were observed by X-ray diffraction analysis. The obtained diffractograms are given in Figs. 1 and 2.

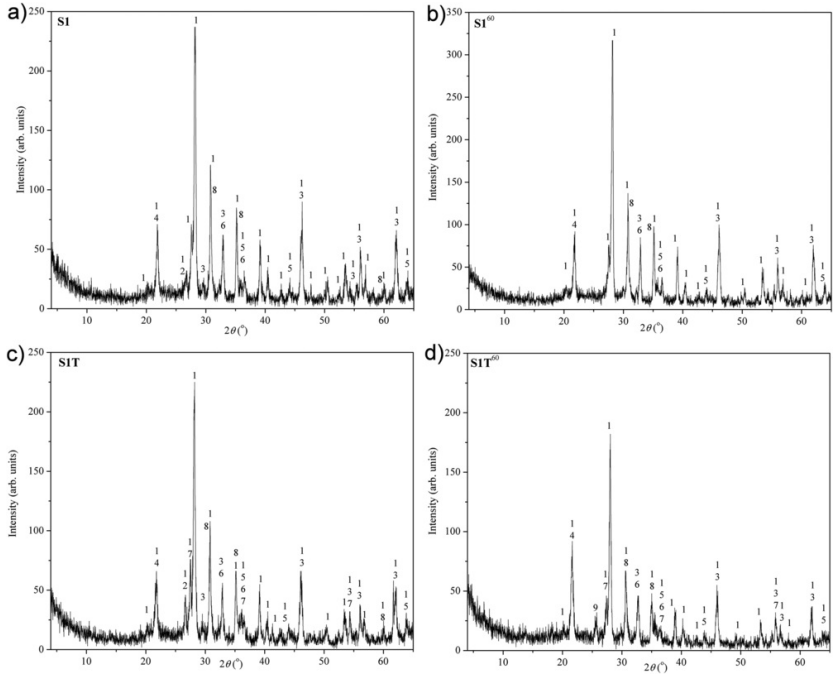


**Fig. 1** The XRD diffractograms of the sintered S1 steatites: a) non-activated mixture; b) activated mixture; c) non-activated mixture with $TiO_2$ and d) activated mixture with $TiO_2$.

alt-text: Fig. 1

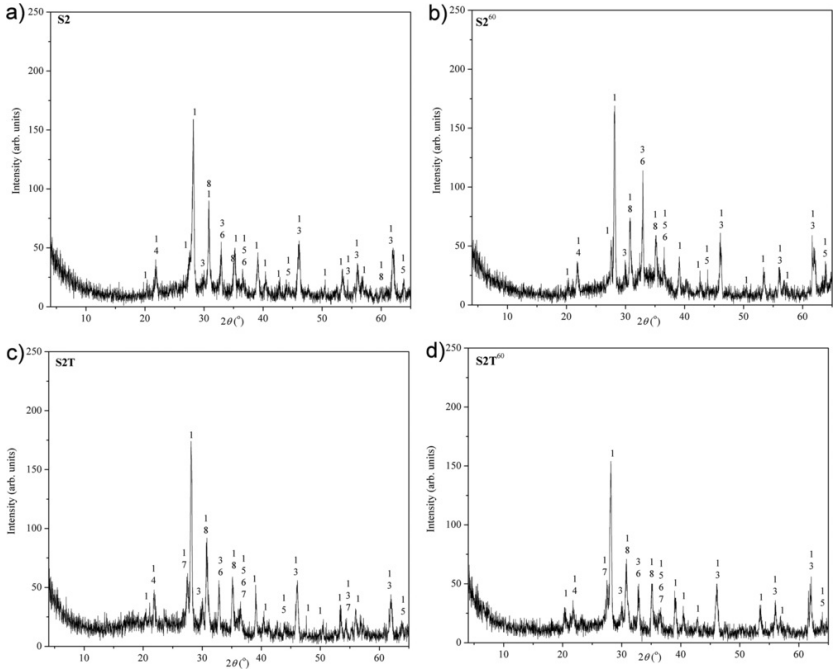

**Fig. 2** The XRD diffractograms of the sintered $S_2$ steatites: a) non-activated mixture; b) activated mixture; c) non-activated mixture with $TiO_2$ and d) activated mixture with $TiO_2$.

alt-text: Fig. 2

The S1 sample comprised the following mineral phases: 1- enstatite ($Mg_2Si_2O_6$; JCPDS 74–0816), 2- quartz ($SiO_2$; JCPDS 46–1045), 3- hibschite ($Ca_3Al_2(SiO_4)_2(OH)_4$; JCPDS 89–4578), 4- cristobalite ($SiO_2$; JCPDS 82–0512), 5- spinel ($MgAl_2O_4$; JCPDS 82–2424), 6- olivine, i.e forsterite ($Mg_2SiO_4$; JCPDS 85–1363) and 8- pyrope ($Mg_3Al_2(SiO_4)_3$, JCPDS 86–0150). The sample S1 activated for ~~60~~60 min ($S1^{60}$ in further text) contained enstatite, hibschite, cristobalite, spinel, olivine and pyrope. The $TiO_2$ doped sample S1T showed the same mineral phase composition as S1, with the additional rutile phase (7; JCPDS 89–4920). The $TiO_2$ doped and ~~60~~60 min activated sample $S1T^{60}$ was also characterized by lack of quartz and presence of rutile, as well as the additional $MgAl_2Si_4O_{12}$ phase, which can be prescribed to the mineral osumilite [40]. The quartz was not detected in neither of the two activated mixtures – $S1^{60}$ and $S1T^{60}$.

The most abundant phase present in all observed steatite samples based on the first mix-design (talc + kaolin clay + feldspar) was enstatite. Enstatite ($Mg_2Si_2O_6$) predominantly originates from talc. When subjected to an increase and/or the cycling of the temperature, enstatite undergoes a series of polymorphic transitions [15,18,20,41]. The complex character of enstatite polymorphism is controlled by various factors: dopants, temperature, pressure, grain sizes, internal stresses in grains, etc. Enstatite occurs in the orthorhombic symmetry at the ambient temperature. Subsequently this mineral passes through a number of polymorphic intermediate structures during the heating: protoenstatite, clinoenstatite, and high-temperature clinoenstatite [42]. While the most of the intermediate polymorphs have a tendency of inversion, protoenstatite is the final stable form of enstatite which usually emerges in the temperature range from ~~1000 °C~~ 1000 °C to ~~1300 °C~~ 1300 °C [43]. The two-step sintering procedure with initial phase set at ~~1350 °C,~~ 1350 °C, and the sintering holding period conducted at ~~1250 °C~~ 1250 °C enabled the formation of predominant protoenstatite phase. The stable enstatite phase was accompanied by other mineral phases detectable only in traces. Therefore all samples based on the first mix-design (i.e. talc – kaolin clay – feldspar) regardless of the $TiO_2$ doping and applied mechano-chemical pretreatment exhibited highly similar mineral compositions. Quartz and cristobalite as polymorphs of silica probably originated from kaolin clay. Cristobalite appears as a more stable crystalline modification of quartz above ~~870 °C,~~ 870 °C, depending on the presence of flux, doping agent and possibly mechano-chemical pretreatment. The XRD analysis (Fig. 1a–d) registered the presence of cristobalite in all observed mixtures upon the conducted two-step sintering. The reflections of cristobalite were feeble and superposed with more significant enstatite peaks in all samples. The activated mixtures (Figs. 1b and 1d) comprised only cristobalite. The former means that the mechanical activation decreased the temperature of quartz transformation by increasing specific surface area of the powder. Namely higher specific surface area enables more contact between particles during the thermal treatment, which enhances their reactivity and finally accelerates the quartz phase transformation. Other phases, such as pyrope ($Mg_3Al_2(SiO_4)_3$), forsterite ($Mg_2SiO_4$), hibschite ($Ca_3Al_2(SiO_4)_2(OH)_4$), and spinel ($MgAl_2O_4$) are products of thermal reactions between oxides of Mg, Al, Si and Ca. These minerals were detected in very small quantities. The rutile phase appeared in the $TiO_2$ doped samples, i.e. S1T and $S1T^{60}$ (Figs. 1c and 1d). Rutile, as a mineral composed primarily of titanium dioxide, is its most common polymorph. The activated and $TiO_2$ doped sample $S1T^{60}$ was also characterized by the presence of the additional $MgAl_2Si_4O_{12}$ phase, i.e. osumilite (Fig. 1d). Osumilite is a member of the milarite mineral group characterized by double hexagonal $(Si, Al)_{12}O_{30}$ rings [40]. This mineral is usually present in glass-ceramics as $MgAl_2Si_4O_{12}$, which corresponds to one $Mg^{2+}$ ion per double unit formula in a channel site, filling only one-quarter of the available channel sites [40]. This metastable phase is usually easily crystallizable from simple ternary glasses [40].

The mineral phase composition of the second steatite mixture (i.e. talc-bentonite-barium carbonate mix) comprised the same phases as the first group of steatites, but with notable variations in the crystallinity of the detected phases. Thereby S2 sample contained: enstatite (1), hibschite (3), cristobalite (4), spinel (5), olivine (6) and pyrope (8). The same phase composition was also detected in the sample activated for ~~60~~60 min ($S2^{60}$). The $TiO_2$ doped steatite mixture (S2T) had additional rutile phase (7), while the $TiO_2$ doped and activated $S2T^{60}$ mixture, besides rutile, showed the presence of osumilite ($MgAl_2Si_4O_{12}$). The most abundant mineral phase in all of the observed samples based on the second mix-design was the stable form of enstatite, i.e. protoenstatite. Cristobalite was the only present polymorph of silica, which presumably originated from bentonite. Other mineral phases (cristobalite, hibschite, spinel, olivine, pyrope, rutile, and osumilite) were detected in traces. Their reflections were mutually overlapped and superposed in the diffractograms in Fig. 2a–d.

The steatite samples based on the first and the second mix-design (Table 1) showed notable differences in the crystallinity of the detected phases. The most significant XRD reflections (Fig. 1a–d and Fig. 2a–d)) are observed in the area between ~~20 °~~ 20° and ~~50 °~~ 50°. Two main peaks corresponding to the stable enstatite polymorph (i.e. protoenstatite) were found at ~~28 °~~ 28° and ~~31 °~~ 31°. The rest of detected peaks represent superposed reflections of enstatite, as the most dominant mineral, with other less abundant mineral phases, as seen in Figs. 1 and 2.

The main enstatite peaks of the sample S1, located at 28° and 31°, showed intensities as high as 230 and 120 arbitrary units (*au* in further text), respectively. The crystallinity of all the other reflections was less then 100 *au*, i.e. between 50 and 100 *au* with a lot of barely detectably peaks (approximately 25 *au*). The activated sample $S1^{60}$ (Fig. 1b) showed a higher intensity of the main peaks (i.e. 320 *au* and 130 *au*) in comparison with S1. The applied mechanical activation increased specific surface area of the treated powder and made it more readily reactive, enabling quicker and more efficient polymorphic transformation and giving the sintered product with a well defined crystalline structure. Analogously, the rest of reflections identified in $S1^{60}$ sample showed a 20–30% higher crystallinity than the corresponding peaks observed in the diffractogram of S1 steatite. The two-step sintering of the $TiO_2$ doped S1T sample (Fig. 1c) gave a less crystalline product in comparison with non-doped mixtures. The intensities of the main reflections at 28° and 31° were 225 *au* and 110 *au*, respectively. Consequently, the rest of peaks were below 75 *au*. The combination of the dopant addition and mechanical pretreatment (sample $S1T^{60}$, Fig. 1d) influenced a further decrease in the crystallinity upon sintering. The intensities of the main reflections were 175 *au* and 60 *au*,

while the rest of the peaks were below 50 *au*. Therefore, the mechanical activation promoted an increase in the crystallinity of the two-step sintered talc-kaolin-feldspar mixture, while the addition of $TiO_2$ induced a small decrease (5–7%) in crystallinity. The combination of $TiO_2$ doping and activation gave a less-developed crystalline structure in the steatite.

The intensities of the two major enstatite peaks of the S2 sample, located at 28° and 31°, were 160 *au* and 90 *au*, respectively. The intensity of the other present reflections was equal or less than 50 *au*, with a lot of barely detectably peaks. The diffractogram of the sample $S2^{60}$ (Fig. 1b) showed somewhat higher intensities of the main reflections: 170 *au* and 110 *au*. The remaining peaks had exactly the same level of crystallinity as the corresponding peaks observed in the diffractogram of S2 steatite. The addition of $TiO_2$ (Fig. 2c) influenced the increase in reflection present at 28° in S2T sample (175 *au*), while the second peak at 31° (90 *au*) was the same as the peak found in the S2 sample. The remaining peaks were less or equal to 50 *au*. The combination of the dopant addition and mechanical activation ($S2T^{60}$, Fig. 1d) led to the highest decrease in the crystallinity of the sintered steatite. The intensities of the main peaks were 155 *au* and 70 *au*, while the remaining reflections were below 50 *au*.

The majority of the reflections detected in both talc-kaolin-feldspar and talc-bentonite-$BaCO_3$ steatites corresponded to the stable enstatite polymorph protoenstatite, accompanied only by the mineral phases detected in traces, which highlights that this sintering route leads to a mineralogically suitable steatite product. Mechano-chemical activation improved the crystallinity of the S1 steatite, while the application of $TiO_2$ as the doping agent led to the same effect during the sintering of S2 steatite. However, the mechanically activated steatite powders with the addition of $TiO_2$ gave sintered samples with comparatively lower crystallinity regardless of the differences in the starting mix-design.

The assessment of the thermal behavior of green steatite powdery mixes was conducted by means of the differential thermal analysis (DTA) and thermogravimetry (TG). The starting steatite mixes S1 and S2 were chosen for the analysis, as well as the activated $S1^{60}$ mix and $TiO_2$ doped S2T mix due to the highest crystallinity exhibited during the XRD testing. The acquired diagrams are presented in Fig. 3.

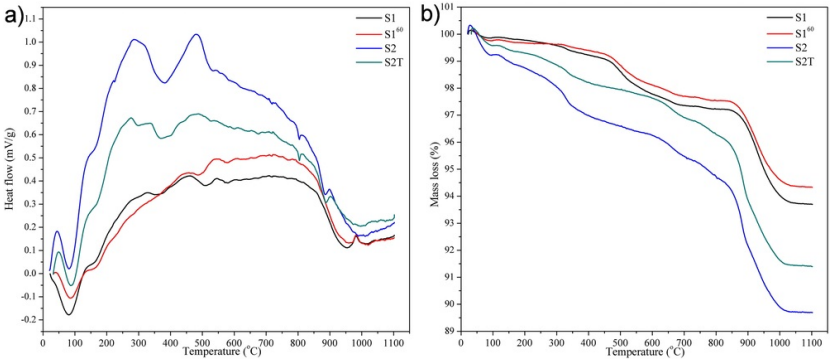


**Fig. 3** Thermal analysis of the steatite powders S1, $S1^{60}$, S2 and S2T: a) differential thermal curves: b) thermogravimetry curves.

alt-text: Fig. 3

Each DTA curve of the investigated steatite mixture (S1, $S1^{60}$, S2 and S2T) comprised three regions: 1) ~~20 °-200 °C,~~ 20–200 °C, 2) ~~200 °-600 °C~~ 200–600 °C and 3) ~~600 °-1110 °C~~ 600–1110 °C (Fig. 3a). These regions fully correspond to the stages of the talc dehydration, because talc is the predominant component in the steatite mix-design. Since talc comprises both adsorbed water and hydroxyl groups that constitute the space lattice elements, the present structural water is driven off in three steps: ~~115 °-200 °C, 350 °-500 °C,~~ 115–200 °C; 350–500 °C, and ~~600 °-1050 °C.~~ 600–1050 °C. These changes are correlated to the endothermic peaks on the talc DTA curve [44].

The first region of the DTA diagram illustrated in Fig. 3a, located between ~~20 °C~~ 20 °C and ~~200 °C,~~ 200 °C, is characterized by a noticeable endothermic effect at approximately ~~75 °C.~~ 75 °C. The exact peak maximum positions are: ~~75.5 °C, 78.3 °C, 78.7 °C,~~ 75.5 °C; 78.3 °C; 78.7 °C; and ~~75.2 °C~~ 75.2 °C for S1, $S1^{60}$, S2T and S2, respectively. Subsequent to the endothermic effect, all DTA curves proceeded into an exothermic hump. There are very small, hardly noticeable effects on the left side of the hump of each curve, located in the proximity of ~~150 °C.~~ 150 °C. Entire initial interval from ~~20 °C~~ 20 °C to ~~200 °C~~ 200 °C can also be regarded as an endothermic valley which is correlated to the first dehydration stage of talc. The areas encompassed by endothermic peaks at ~~75 °C~~ 75 °C are approximately the same for all four observed steatite mixtures, which contributes to the presumption that all initial effects are correlated solely to the talc dehydration.

The differential thermal analysis highlighted the second region ~~(200 °-600 °C)~~ (200–600 °C) which is marked by more significant differences between the observed steatite samples. The S1 sample showed three very small endothermic effects with maxima located at: ~~351.2 °C, 498.4 °C~~ 351.2 °C; 498.4 °C and ~~556.5 °C.~~ 556.5 °C. These effects are part of the background exothermic hump. The first two peaks correspond to the further dehydration of talc (i.e. the second stage of talc decomposition). They are hardly noticeable because during the initial two stages of talc decomposition only 0.4% of water is liberated [44]. The effect, located at ~~556.5 °C~~ 556.5 °C can be correlated to the quartz

transformation, i.e. transition of α-quartz into β-quartz modification, which normally takes place at ~~573~~573 °C in pure $SiO_2$ [44,45]. As the XRD analysis illustrated, quartz is present only in moderate quantity, which resulted in relatively unnoticeable changes in the crystalline structure of steatite S1 and an equally small effect on the DTA curve. The mechanically activated $S1^{60}$ sample showed a very similar DTA curve to that of the S1 steatite. The activation promoted creation of more amorphous (i.e. glassy) phase which led to the elevation of the curve base line in comparison with the diagram obtained for the S1 sample. This was especially noticeable for the streaming of S1 and $S1^{60}$ curves at temperatures above ~~350 °C.~~ 350 °C. The DTA diagram of $S1^{60}$ steatite exhibited two endothermic effects in the second region located at ~~475.1 °C~~ 475.1 °C and ~~554.8 °C.~~ 554.8 °C. The S2 steatite mixture showed a very pronounced endothermic effect in the ~~275 °C to 480 °C~~ 275–480 °C zone. The peak of this effect was located at ~~375.2 °C.~~ 375.2 °C. This effect can be correlated with addition of bentonite as bonding agent to the mix-design. Namely, bentonite, i.e. its main mineral montmorillonite, undergoes one-step dehydration that takes place from ~~100 °C~~ 100 °C to ~~450 °C.~~ 450 °C. During this process the most of the hydration water from bentonite is eliminated, which is marked by a sequence of thermal reactions, i.e. effects on the bentonite DTA curve [46]. According to the trend of the curve of the S2T steatite in the second region, the addition of $TiO_2$ made effects related to montmorillonite dehydration more subtle. The thermal reactions that took place in the second region induced the formation of extra amount of glassy phase in talc–bentonite–$BaCO_3$ steatites in comparison to talc–feldspar–kaolin mixes.

The streaming of the curves in the third region of the thermal analysis diagram ~~(600 °–1110 °C)~~ (600–1110 °C) is relatively similar for all four steatite samples. Namely, all diagrams proceeded into endothermic valley, whose lowest point is set at approximately ~~1000 °C.~~ 1000 °C. During this stage the remaining 5.1% of the total non-hygroscopic water from talc is being removed [44]. All curves exhibited several small either endothermic or exothermic peaks. These peaks can be correlated to the crystallization of magnesium metasilicate. Namely, talc decomposes into magnesium oxide and silica due to the liberation of constitution water [44,45]. These reactions would take place at approximately ~~800 °C~~ 800 °C in pure talc; however the activation pretreatment, as well as fluxing and doping agents inevitably altered the reaction route. Above ~~800 °C,~~ 800 °C, the recrystallization within talc structure and formation of the stable enstatite polymorph are taking place. Also in this interval (i.e. around ~~950 °C)~~ 950 °C) the crystallization of silica (i.e. quartz) and its transition into cristobalite takes place. Thereby, the observed curves had several small peaks related to the mentioned phase transformation, i.e. S1 and $S1^{60}$ samples showed small exothermal peaks at approximately ~~990 °C,~~ 990 °C, while S2 and S2T exhibited two endothermic peaks. The first peak appeared at ~~800 °C~~ 800 °C and the second was at ~~880 °C.~~ 880 °C. The minimum located at ~~1000 °C~~ 1000 °C can be adopted as temperature of the crystallization of the stable enstatite polymorph – protoenstatite. Further heating contributes to the creation of a well-ordered crystalline structure and establishment of the stable enstatite polymorph as the predominant mineral phase in the steatite composition, as the results of the XRD analyses showed.

The results of the thermogravimetric analysis are illustrated in Fig. 3b. During the initial stage of the heating from ~~20 °C~~ 20 °C to ~~200 °C,~~ 200 °C, the TG diagrams of S2 and S2T steatite powders showed a small initial mass loss counting up to 1.25% and 0.75%, respectively. The diagrams of the S1 and $S1^{60}$ samples exhibited infinitesimal mass loss (0.25%). These changes correspond to the first dehydration stage of talc.

Following the pattern of the differential thermal analysis, the second thermal region was set in the interval from ~~200 °C~~ 200 °C to ~~600 °C.~~ 600 °C. Registered mass losses in this interval were higher in comparison with the initial stage. They are predominantly related to the second phase of talc dehydration. S2 steatite showed the highest mass loss: 3.35%. The mass loss values registered for the remaining samples were relatively similar: 1.85%, 1.65% and 1.5% for S1, $S1^{60}$ and S2T, respectively. The samples which comprised kaolin clay and feldspar (S1 and $S1^{60}$) showed a small effect, i.e. convex hump, located at approximately ~~500 °C,~~ 500 °C, which can be correlated to the α- to β-quartz transformation [45,46]. The samples S2 and S2T, which contained bentonite as the bonding agent, exhibited relatively small concave valley at ~~350°C~~350 °C on the TG curve. This effect is the result of one-step dehydration of bentonite main mineral montmorillonite [46,47].

During the third thermal region, TG curves of the investigated steatite mixtures showed differences due to variations in their mix-design. The samples S1 and $S1^{60}$ showed the two step mass loss in ~~600 °–1100 °C~~ 600–1100 °C interval. The mass loss registered from ~~600 °C~~ 600 °C to ~~850 °C~~ 850 °C was 0.5% and 0.4% for S1 and $S1^{60}$ steatite mixes, respectively. The change in the mass of samples detected from ~~850 °C~~ 850 °C to ~~1100 °C~~ 1100 °C summed up to 3.5% for S1 and 3.1% for $S1^{60}$. The mechanically pre-treated sample showed smaller mass loss during the final thermal stage, as well as the total mass change measured from ambient to the maximal temperature of the thermal treatment, i.e. 5.4% for $S1^{60}$ and 6.1% for S1. Unlike talc-feldspar-kaolin steatites, S2 steatites showed one step mass loss during the final stage. The mass loss of S2 sample was 6.6%, while $TiO_2$ doped mixture resulted with a smaller mass loss (6.1%) during the third stage. The total mass loss for samples S2 and S2T summed up to 11.2% and 8.3%. The additions of bentonite binder and barium carbonate flux led to a higher mass loss in steatite, but the application of $TiO_2$ dopant induced a decrease in the mass loss. The changes in the third region of the TG diagram can be correlated to the final and most intense stage of talc dehydration. The changes that took place at approximately ~~850 °C~~ 850 °C are related to the cristobalite crystallization from the initial silica and the magnesium metasilicate transformations. The interval from ~~850 °C~~ 850 °C to ~~1100 °C~~ 1100 °C can be considered as a period when the transformation of enstatite into its stable polymorph is taking place.

The SEM microstructural analysis was conducted on the parts of the crushed and non-polished steatite samples S1, $S1^{60}$, S2 and S2T, upon the conducted two-step sintering. The SEM micro-photographs are given in Fig. 4.

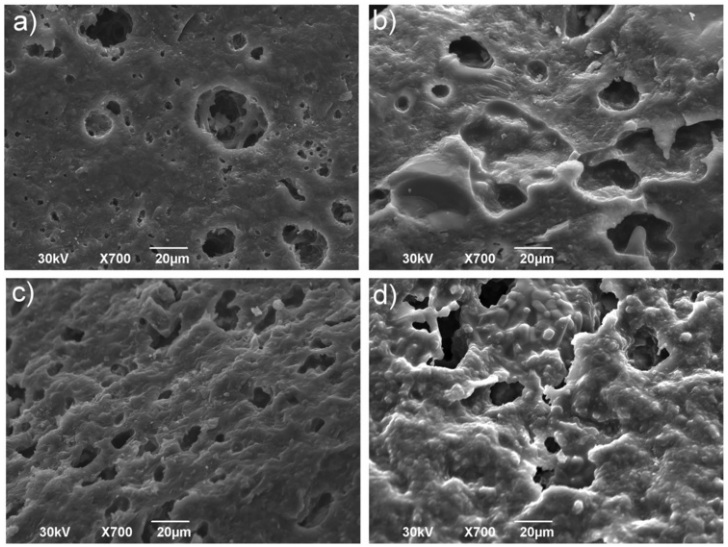


**Fig. 4** The SEM analysis of steatite samples: a) S1; b) $S1^{60}$; c) S2 and d) S2T.

alt-text: Fig. 4

Talc, as the base resource material for the steatite synthesis provided characteristic shell-like silicate structure with triclinic symmetry [34] in all investigated samples. The increase in the sintering temperature may influence certain disadvantageous occurrences within the talc structure such as formation of micropores (sizing approximately ~~500~~500 Å) and release of free quartz [8]. The application of $TiO_2$ dopant as well as the mechanical pre-treatment contributed to the prevention of microporosity development (Fig. 4b and c). According to the XRD results (Fig. 1 and 2), quartz in its primary modification was present only in the sample S1 upon conducted two-step sintering. The rest of the steatites comprised stable quartz polymorph – cristobalite, which was present in minor quantity, i.e. within detection limits. As it can be seen from the microphotographs in Fig. 4., orthorhombic enstatite transitioned into stable protoenstatite crystals which are surrounded by a glassy matrix forming a solid ceramic structure.

The S1 steatite sample (Fig. 4a), comprised a mixture of angular and irregularly shaped particles. These crystalline particles were submerged in amorphous matter thus creating a form of micro-reinforcement for the structure of the investigated ceramic material. The particles were very small, predominantly sizing from ~~2.0 μm~~ 2.0 μm to ~~7.0 μm.~~ 7.0 μm. Their average size is less then ~~10 μm,~~ 10 μm, which is considered as the upper dimensional limit for the stable enstatite polymorph – protoenstatite [18,20]. Thereby the recorded particles predominantly correspond to the protoenstatite mineral. This is in agreement with the diffractogram recorded upon the two-step sintering (Fig. 1a). Protoenstatite is normally characterized by relatively massive prismatic crystals [8] which is endorsed by the hereby presented microphotograph. The crystals of protoenstatite can also exhibit a lamellar or fibrous structure [8]. A cluster of massive, lamellarly constituted particles can be seen in the middle of the SEM microphotograph (Fig. 4a.) situated within the huge superficial voids. These several superficial voids, with diameters sizing from ~~15.37 μm~~ 15.37 μm to ~~37.79 μm~~ 37.79 μm are a result of the mechanical crushing of the previously tableted and sintered steatite mixtures. However, the superficial voids revealed the internal porosity as well as channels formed by merging of the pores and cavities. Thereby, the created grain boundaries between protoenstatite particles are relatively feeble at various places in the steatite structure because the ceramic material is intersected with channels. Such material presumably results in low hardness and physico-mechanical properties. Other mineral phases detected by the X-ray diffraction analysis (e.g. quartz, cristobalite, pyrope, hibschite, etc.) were in extremely low amounts; therefore they could not be registered in the microphotograph. Also, the microstructural analysis of the S1 sample pointed out to a slightly increased porosity. Pores were relatively small with diameters ranging from below ~~1.0 μm to 4.25 μm.~~ 1.0–4.25 μm. The average pore size was approximately ~~2.30 μm.~~ 2.30 μm. The pores were set between particles, as the result of imperfect packing and slightly deficient amount of amorphous phase. The observed submicro voids did not appear on the particles, which rules out the possibility of formation of micropores, which are the previously mentioned as a negative result of the talc decomposition. The steatite structure obtained upon the two-step sintering did not comprise signs of structural cracking or similar defects.

The mechanically activated sample $S1^{60}$ (Fig. 4b) acquired a very similar structure as the corresponding S1 sample based on the same mix-design (talc–kaolin–feldspar). Protoenstatite angular crystals were submerged in the glassy phase. The crystals are very small, sizing ~~2.0–3.0 μm.~~ 2.0–3.0 μm. The mechano-chemical activation as a pretreatment of the powdery material contributed to the reactivity between phases and creation of an extra amount of amorphous substance which filled in the pores thus reducing the microporosity. Superficial voids, created during crushing of the samples, show solid material with absence of internal channels or voids.

The sample S2 which comprised talc, barium carbonate and bentonite in its mix-design produced a coarser and more porous structure than the steatites based on the first mix-design, as it can be seen in Fig. 4c. The particles are sizing from ~~7.0 μm~~ 7.0 μm to ~~9.0 μm,~~ 9.0 μm, which still dimensionally qualifies them as the stable protoenstatite polymorph (i.e. average size of a polymorph crystal ≤ ~~10 μm).~~ 10 μm). The crystals are well submerged in the glassy phase, but the superficial porosity is increased and pores are bigger in comparison with previous samples. The diameters of the superficial pores are ranging from ~~3.73 μm~~ 3.73 μm to ~~7.61 μm.~~ 7.61 μm. The relatively high open porosity present in S2 sample upon the two-step sintering is a consequence of the application of $BaCO_3$ as fluxing agent. Namely, it is highly probable that gaseous carbon dioxide from $BaCO_3$ was released during high-temperature reactions and thereby contributed to the formation of the additional share of pores. In the structure, the present pores were shallow, indicating no presence of internal channels made of merged voids and cavities.

The S2T steatite mixture doped with $TiO_2$ produced a structure composed of well-merged protoenstatite particles and glassy phase (Fig. 4d). The amount of amorphous matter was the highest in comparison with the previous samples, because $TiO_2$ additionally decreased the temperature of sintering. The protoenstatite particles were coarser in comparison with $S1^{60}$ sample, because this mixture was not submitted to the activation pre-treatment. Therefore, the average size of the mineral particles was ~~5–6 μm.~~ 5–6 μm. The protoenstatite particles were more round than angular due to the change in shape during prolonged sintering. Namely, the application of dopant decreased sintering temperature and thereby induced its early start, and consequently extended the period of sintering in already pre-determined two-step procedure route. Additional effect was the creation of well formed and highly compact structure. Despite utilization of $BaCO_3$ as flux, the extended sintering period prevented the formation and release of the gas phase. Therefore, the increased porosity, characteristic for S2 steatite, is absent from the S2T microstructure. The superficial voids caused by crushing of the sample, showed absence of internal pore channels.

The EDS analysis of the characteristic points in the SEM microphotographs (from Fig. 4) is given in Fig. 5. The elemental analysis is provided in Table 3.

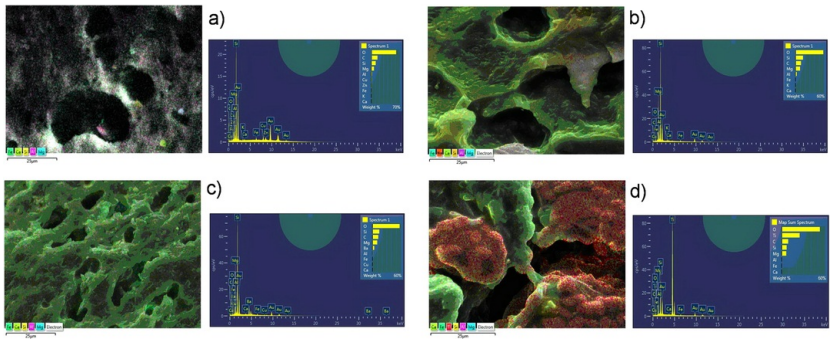


**Fig. 5** EDS mapping (left) and diagram of element analysis (right) of the steatite samples: a) S1; b) $S1^{60}$; c) S2 and d) S2T.

alt-text: Fig. 5

**Table 3** EDS elemental analysis of steatite samples[a].

alt-text: Table 3

| Element | Apparent concentration | k Ratio | wt% | Element | Apparent concentration | k Ratio | wt% |
|---|---|---|---|---|---|---|---|
| **S1** | | | | **$S1^{60}$** | | | |
| C | 1.68 | 0.01677 | 15.52 | C | 3.54 | 0.03538 | 12.69 |
| O | | | 61.01 | O | | | 59.65 |
| Mg | 3.65 | 0.02423 | 7.07 | Mg | 15.30 | 0.10146 | 9.23 |
| Al | 1.00 | 0.00717 | 1.77 | Al | 4.30 | 0.03088 | 2.49 |
| Si | 8.08 | 0.06401 | 11.39 | Si | 30.71 | 0.24335 | 14.63 |
| K | 0.16 | 0.00133 | 0.15 | Na | 0.72 | 0.00302 | 0.46 |
| Ca | 0.15 | 0.00137 | 0.14 | K | 0.70 | 0.00594 | 0.23 |
| Fe | 0.58 | 0.00580 | 0.49 | Ca | 0.43 | 0.00383 | 0.16 |

| | | | | | | | |
|---|---|---|---|---|---|---|---|
| | | | | Fe | 0.84 | 0.00837 | 0.25 |
| | | | | Zr | 0.15 | 0.00153 | 0.21 |
| | | | | | | | |
| **S2** | | | | **S2T** | | | |
| C | 3.18 | 0.03185 | 12.23 | C | 2.68 | 0.02685 | 8.95 |
| O | | | 57.44 | O | | | 52.59 |
| Mg | 14.77 | 0.09796 | 10.32 | Mg | 6.42 | 0.04259 | 6.22 |
| Al | 1.23 | 0.00887 | 0.86 | Al | 0.44 | 0.00316 | 0.36 |
| Si | 26.43 | 0.20943 | 14.52 | Si | 10.57 | 0.08375 | 6.74 |
| Ca | 0.40 | 0.00356 | 0.14 | Ca | 0.19 | 0.00171 | 0.07 |
| Fe | 0.80 | 0.00804 | 0.31 | Ti | 55.15 | 0.55149 | 21.13 |
| Ba | 10.70 | 0.10024 | 3.90 | Ba | 10.70 | 0.10024 | 3.60 |
| | | | | Fe | 0.71 | 0.00715 | 0.34 |

[a] Au was eliminated from elemental analysis.

The conveyed EDS analyses fully support the results of the chemical analysis (Table 1) and the mineral-phase investigation (Figs. 1 and 2) of the steatite samples. Silicon and magnesium were two most abundant chemical element detected in the investigated samples, as it can be seen from Fig. 5 and Table 4. Apparent concentration and weight percentage of Mg were ~~3.65~~3.65% and 7.07%, ~~15.30~~15.30% and 9.23%, ~~14.77~~14.77% and 10.32%, ~~6.42~~6.42% and 6.22% in S1, S1$^{60}$, S2 and S2T, respectively. The mentioned parameters determined for Si were: ~~8.08~~8.08% and 11.39%, ~~30.71~~30.71% and 14.63%, ~~26.43~~26.43% and 14.53%, ~~10.57~~10.57% and 6.74%, in S1, S1$^{60}$, S2 and S2T, respectively. Silicon and magnesium are chemically bonded in magnesium silicate, which represents talc in its stable and the most abundant mineral phase protoenstatite. Aluminum is present in relatively small quantity (1.0 & 1.77% in S1; 4.30 & 2.49% in S1$^{60}$; 1.23 & 0.86% in S2, and 0.44 & 0.36% in S2T). The present aluminum predominantly originates from the used binder kaolin clay in the first mixture or bentonite in the second mixture. The comparison of the samples S1 and S1$^{60}$ highlighted the increase in the most abundant elements – Si, Mg and Al. Since the starting mix-design of these samples was the same, it can be assumed that mechano-chemical pretreatment enhanced reactivity of $SiO_2$, MgO and $Al_2O_3$ by such increasing the quantity of the products of their reactions in the final two-step sintered product. The non-treated sample with addition of $TiO_2$ dopant showed the opposite correlation, namely concentrations of Si, Al, and Mg decreased upon thermal treatment. The percentage of elemental oxygen is in the range from 52% to 61% in all observed samples. This element is chemically bonded in various oxides. Potassium, sodium, calcium, and iron are present in very small amounts. Namely their quantities are either not surpassing 1% or they are below level of detection. Certain low amount of Zr was detected in the sample S1$^{60}$ due to the applied pre-treatment in planetary mill with Zr grinding balls. Significant amount of Ti was present in the sample S2T due to $TiO_2$ high temperature reactions during sintering which resulted in additional amount of glassy phase.

**Table 4** Dielectric properties of steatite samples at ~~96~~96 MHz.

alt-text: Table 4

| Sample | Activation time, min | $\varepsilon_r$ | tan δ |
|---|---|---|---|
| **S1** | 0 | 4.567 | 0.002 |
| | 30 | 5.032 | 0.002 |
| | 45 | 4.952 | 0.002 |
| | 60 | 5.039 | 0.002 |
| **S1T** | 0 | 3.610 | 0.002 |
| | 30 | 4.548 | 0.002 |
| | 45 | 4.899 | 0.002 |

| | | | |
|---|---|---|---|
| | 60 | 4.240 | 0.002 |
| **S2** | 0 | 4.578 | 0.001 |
| | 30 | 4.543 | 0.001 |
| | 45 | 4.350 | 0.001 |
| | 60 | 4.650 | 0.001 |
| **S2T** | 0 | 4.247 | 0.001 |
| | 30 | 3.655 | 0.001 |
| | 45 | 3.506 | 0.001 |
| | 60 | 3.603 | 0.001 |

The EDS elemental mapping in the SEM images (Fig. 5~~a-d~~a–d) gave a closer insight into spatial arrangement of individual chemical elements on the surface of the recorded two-step sintered steatite samples S1, S1[60], S2 and S2T. The majority of the element-related dots in the microphotographs can be related to Mg and Si which originate from protoenstatite. These elements are over-lapping as they are homogenously distributed on all surfaces of the samples in the microphotographs. Aluminum dots are distributed within the close-gapped greed of Mg and Si points, representing oxides which can be related to the bentonite or kaolin clay binders. Ti dots are clearly visible on parts of the S2T surface (Fig. 5d). Titanium is especially evenly distributed in the areas with visibly increased glassy/amorphous phase, which are surrounded by crystalline protoenstatite particles (Mg and Si rich zones).

The dielectric properties were evaluated for the steatite samples based on two different mix-designs (Table 1). The influence of different mechano-activation periods and the addition of $TiO_2$ dopant on the dielectric parameters measured after the conducted two-step sintering was monitored. The relative permittivity was practically independent of frequency. The loss tangent was small, at the threshold of the measurements (0.001), and it slowly increased with frequency. As a representative case, Table 4 shows the results obtained for ~~96~~96 MHz. Based on the analysis of the measurement system, the highest accuracy is obtained in the frequency range from ~~50~~50 MHz to ~~200~~200 MHz. A single frequency, i.e. the frequency of ~~96~~96 MHz was chosen as the representative one, because it is near the middle of the given range, observed on a logarithmic scale.

The low loss tangent qualifies the synthesized steatites as good dielectric materials in electrical engineering. The loss tangent (0.002) was about two times higher for the samples based on the first mix-design (talc-kaolin-feldspar) than for the samples based on the second mixture (talc-bentonite-$BaCO_3$).

The top and bottom surfaces of the samples were not metallized because the electrodes were provided by the construction of the coaxial chamber. However, these surfaces were not perfectly plan-parallel, which increased the measurement error. The estimated measurement error for the relative permittivity is 2%. Taking into account this error, we can conclude that the relative permittivity of the S1 sample increased with the duration of the activation pre-treatment. The highest $\varepsilon_r$ was obtained for the sample S1 that was mechanically activated for ~~60~~60 min prior to the sintering. It has been widely found and accepted that higher initial densities, which result from the activation treatment, lead to better sintered products and the enhancement of the dielectric constant. The sintering initiates further microstructural changes and rearrangements, affecting the density and the amount of open and closed pores. Both processes have a significant influence on the permittivity, which is the crucial characteristic for insulation ceramic materials [48]. The non-activated steatite S1 doped with $TiO_2$ (S1T) exhibited a lower relative permittivity than S1. Similarly, $\varepsilon_r$ of the activated S1T samples was lower than of the corresponding activated S1 samples.

The mechanical activation of the S2 samples had a small influence on the relative permittivity. The combination of activation and doping with $TiO_2$ of the steatite S2 mixture caused a decrease of the relative permittivity.

# 4 Conclusion

This study gave an insight to the mutual interrelations among the two-step sintering route, crystalline development, thermal, microstructural and dielectric behavior of the steatite ceramics, with mix-design based on the economic resources, in regard to the mechanical pretreatment and the application of $TiO_2$ as the doping agent.

Investigated steatites showed a tendency for establishing the mono-phase protoenstatite composition during the thermal treatment. Hibschite, cristobalite, spinel, olivine and pyrope appeared in traces. Rutile and osumilite were in detection limits in the $TiO_2$ doped steatites. The activation improved the crystallinity of protoenstatite in S1 system, while $TiO_2$ dopant had similar effect in the S2 mix. The steatites exhibited thermal behavior analogous to the route of the three-stage dehydration of talc. The DTA effects located above ~~850°C~~850 °C highlighted the re-crystallization of magnesium-silicate and formation of the stable protoenstatite. The activation promoted creation of glassy phase in the S1 (talc–feldspar–kaolin) steatite. $TiO_2$ reduced the glassy phase amount in S2 (talc–bentonite–$BaCO_3$) steatites. The mechanical pre-treatment as well as the application of $TiO_2$ dopant contributed to the prevention of the microporosity development and the creation of pore chanels within the steatite microstructure. The mechanically pre-treated S1 sample, as well as $TiO_2$ doped mixture S2 resulted with a smaller mass loss during thermal treatment.

The loss tangent was two times higher for the samples with the first mix-design than for the samples based on the second mixture. The relative permittivity of the S1 steatite increased with the duration of the activation pre-treatment. The non-treated steatite S1 doped with $TiO_2$ showed a lower relative permittivity than S1. The mechanical activation of the S2 samples had a small influence on the relative permittivity. The combination of activation and doping with $TiO_2$ of the steatite S2 mixture caused a decrease of the relative permittivity. The low dielectric loss tangent categorizes all investigated steatites as good dielectric materials in electrical engineering.


## Acknowledgements ( The corrected text for the Acknowledgments should be as listed here: This investigation was supported by the Ministry of Education, Science and Technological Development of the Republic of Serbia. The research was conducted under the following projects: ON 172057 (Directed synthesis, structure and properties of multifunctional materials) and III 45008 ( Development and application of multifunctional materials based on domestic raw materials by modernization of traditional technologies). The authors would like to express their gratitude to Dr. Smilja Marković, Institute of Technical Sciences of SASA, Belgrade, Serbia, for providing help with the thermal analysis)

This investigation was supported by the Serbian Ministry of ~~Education~~Education, Science and Technological Development~~, Science~~ and it was conducted under the following projects: ON 172057 and III 45008~~III 45008.~~ .The authors would like to express their gratitude to Dr. Smilja Marković, Institute of Technical Sciences of SASA, Belgrade, Serbia, for providing help with the thermal analysis.


## References


**[1]** E. Vela, M. Peiteado, F. Garcia, A. Caballero and J. Fernandez, Sintering behaviour of steatite materials with barium carbonate flux, *Ceram. Int.* **33**, 2007, 1325–1329.

**[2]** J. Liebermann, Microstructure, properties and product quality of strength stressed high voltage insulators, *Am. Ceram. Soc. Bull.* **82**, 2003, 39–46.

**[3]** M. Valaškov, J. Zdrálková, J. Tokarský, G. Martynková, M. Ritz and S. Študentová, Structural characteristics of cordierite/steatite ceramics sintered from mixtures containing pore-forming organovermiculite, *Ceram. Int.* **40**, 2014, 15717–15725.

**[4]** A. Terzić, Lj Andrić, J. Stojanović, N. Obradović and M. Kostović, Mechanical activation as sintering pre-treatment of talc for steatite ceramics, *Sci. Sinter.* **46**, 2014, 247–258.

**[5]** Y. Dong, B. Sosna, O. Korup, F. Rosowski and R. Horn, Investigation of radial heat transfer in a fixed-bed reactor: ~~CFD~~cfd simulations and profile measurements, *Chem. ~~Engin.~~Eng. J.* **317**, 2017, 204–214.

**[6]** T. Tian, L. Cheng, J. Xing, L. Zheng and G. Li, Effects of sintering on the microstructure and electrical properties of ZnO-based thermoelectric materials, ~~*Materials & Design*~~*Mater. Des.* **132**, 2017, 479–485.

**[7]** E. Śnieżek, J. Szczerba, P. Stoch, R. Prorok and E. Burkel, Structural properties of ~~MgO-ZrO2~~MgO-$ZrO_2$ ceramics obtained by conventional sintering, arc melting and field assisted sintering technique, ~~*Materials & Design*~~*Mater. Des.* **99**, 2016, 412–420.

**[8]** W. Mielcarek, D. Nowak-Woźny and K. Prociów, Correlation between $MgSiO_3$ phases and mechanical durability of steatite ceramics, *J. Eur. Ceram. Soc.* **24**, 2004, 3817–3821.

**[9]** S. Berretta, K.E. Evans and O.R. Ghita, Predicting processing parameters in high temperature laser sintering (HT-LS) from powder properties, ~~*Materials & Design*~~*Mater. Des.* **105**, 2016, 301–314.

**[10]** Z. Zhang, Y. Yi, X. Wang, J. Guo and S. Zhang, A comparative study of progressive wear of four dental monolithic, veneered glass-ceramics, *J. Mech. Behav. Biomed. Mater.* **74**, 2017, 111–117.

**[11]** H. Zhawi, M. Kaizer, A. Chughtai, R. Moraes and Y. Zhang, Polymer infiltrated ceramic network structures for resistance to fatigue fracture and wear, ~~*Dental*~~*Dent. Mater.* **32**, 2016, 1352–1361.

**[12]** M. Ghazal, B. Yang, K. Ludwig and M. Kern, Two-body wear of resin and ceramic denture teeth in comparison to human enamel, ~~*Dental*~~*Dent. Mater.* **24**, 2008, 502–507.

**[13]** P. Rohana. Neufuss, J. Matejícek, J. Dubský, L. Prchlık and C. Holzgartner, Thermal and mechanical properties of cordierite, mullite and steatite produced by plasma spraying, *Ceram. Int.* **30**, 2004, 597–603.

**[14]** J. Croquesel, D. Bouvard, J. Chaix, C. Carry and S. Saunier, Development of an instrumented and automated single mode cavity for ceramic microwave sintering: ~~Application~~application to an alpha pure alumina powder ~~*Materials & Design*~~*Mater. Des.* **88**, 2015, 98–105.

**[15]** J. Jiao, X. Liu, W. Gao, C. Wang, H. Feng, X. Zhao and L. Chen, Two-step synthesis of witherite and tuning of morphology, *Mater. Res. Bull.* **45**, 2010, 181–185.

**[16]** A. Terzić, N. Obradović, J. Stojanović, V. Pavlović, Lj Andrić, D. Olćan and A. Đorđević, Influence of different bonding and fluxing agents on the sintering behavior and dielectric properties of *steatite* ceramic materials,

*Ceram. Int.* **43**, 2017, 13264–13275.

**[17]** H. Gökce, D. Agaogulları, M. Lütfiovecoglu, I. Dumana and T. Boyraz, Characterization of microstructural and thermal properties of steatite/cordierite ceramics prepared by using natural raw materials, *J. Eur. Ceram. Soc.* **31**, 2011, 2741–2747.

**[18]** J.V. Smith, The crystal structure of protoenstatite, $MgSiO_3$, *Acta ~~Crystallographica~~Crystallogr.* **12**, 1959, 515–519.

**[19]** W. Lee and A. Heuer, On the polymorphism of enstatite, *J. Am. Ceram. Soc.* **70**, 1987, 349–360.

**[20]** B. Reynard, J.D. Bass and J.M. Jackson, Rapid identification of steatite–enstatite polymorphs at various temperatures, *J. Eur. Ceram. Soc.* **28**, 2008, 2459–2462.

**[21]** P. Ptáceka, K. Lang, F. Soukal, T. Opravil, E. Bartonícková and L. Tvrdík, Preparation and properties of enstatite ceramic foam from talc, *J. Eur. Ceram. Soc.* **34**, 2014, 515–522.

**[22]** A. Goel, D. Tulyaganov, S. Agathopoulos, M. Ribeiro and J. Fereirra, Synthesis and characterization of $MgSiO_3$ containing glass-ceramics, *Ceram. Int.* **33**, 2007, 1481–1487.

**[23]** N. Lóh, L. Simão, C. Faller, A. DeNoni, Jr and O. Montedo, A review of two-step sintering for ceramics, *Ceram. Int.* **42**, 2016, 12556–12572.

**[24]** J. Nie, Y. Zhang, J.M. Chan, S. Jiang, R. Huang and J. Luo, Two-step flash sintering of ZnO: ~~Fast~~fast densification with suppressed grain growth, *~~Scripta Materialia~~Scr. Mater.* **141**, 2017, 6–9.

**[25]** S. Kumar, K. Ananthasivan, A. Senapati, S. Amirthapandian and A. Dasgupt, Nitrate fusion synthesis and two-step sintering of nanocrystalline yttria stabilized hafnia powders, *Ceram. Int.* **44**, 2018, 7393–7405.

**[26]** J. Zhang, Y. Zheng, J. Chen, W. Zhou, Y. Zhao and P. Feng, Microstructures and mechanical properties of Mo2FeB2-based cermets prepared by two-step sintering technique, *Inter. J. Refract. ~~Metals~~Met. Hard ~~Mate.~~Mater.* **72**, 2018, 56–62.

**[27]** U. Sutharsini, M. Thanihaichelvan, C.H. Ting, S. Ramesh, C.Y. Tan, H. Chandran, A. Sarhan, S. Ramesh and I. Urriés, Effect of two-step sintering on the hydrothermal ageing resistance of tetragonal zirconia polycrystals, *Ceram. Int.* **43**, 2017, 7594–7599.

**[28]** N. Lóh, L. Simão, J. Jiusti, A. Noni and O. Montedo, Effect of temperature and holding time on the densification of alumina obtained by two-step sintering, *Ceram. Int.* **43**, 2017, 8269–8275.

**[29]** I.W. Chen and X.H. Wang, Sintering dense nano crystalline ceramics without final stage grain growth, *Nature* **404**, 2000, 168–171.

**[30]** X. Wang, P. Chen and I. Chen, Two step sintering of ceramics with constant grain-size, I.$Y_2O_3$, *J. Am. Ceram. Soc.* **89**, 2006, 431–437.

**[31]** B. Wang, J. Du, Y. Liu and G. Yao, Effect of $TiO_2$ ~~Doping~~doping on the ~~Sintering Process, Mechanical~~sintering process, mechanical and ~~Magnetic Properties~~magnetic properties of $NiFe_2O_4$ ~~Ferrite Ceramics~~ferrite ceramics, *Appl. Ceram. ~~Tech.~~Technol.* **12**, 2015, 658–664.

**[32]** E. Sentürk, S. Duman, S. Bagcıa, H.S. Soykan and Z. Aslanogluca Sakarya, Humidity sensing properties of steatite ceramic containing $B_2O_3$, *~~Sensors and~~ Sens. Actuators A* **240**, 2016, 80–84.

**[33]** L. Zhang, S. Olhero and J. Ferreira, Thermo-mechanical and high-temperature dielectric properties of cordierite-mullite-aluminaceramics, *Ceram. Int.* **42**, 2016, 16897–16905.

**[34]** A. Benhammou, Y. El Hafiane, A. Abourriche, Y. Abouliatim, L. Nibou, A. Yaacoubi, N. Tessier-Doyen, A. Smith and B. Tanouti, Influence of sintering temperature on the microstructural and mechanical properties of cordierite synthesized from andalusite and talc, *Mater. ~~Letters~~Lett.* **172**, 2016, 198–201.

**[35]** Y. Liu, F. Luo, J. Su, W. Zhou, D. Zhu and Z. Li, Enhanced mechanical, dielectric and microwave absorption properties of cordierite based ceramics by adding $Ti_3SiC_2$ powders, *J. ~~Alloys~~Alloy. Comp.* **619**, 2015, 854–860.

**[36]** N. Obradović, S. Filipović, N. Đorđević, D. Kosanović, S. Marković, V. Pavlović, D. Olćan, A. Đordjević, M. Kachlik and K. Maca, Effects of mechanical activation and two-step sintering on the structure and electrical properties of cordierite-based ceramics, *Ceram. Int.* **42**, 2016, 13909–13918.

**[37]** H. Li, Z. Huang, L. Cheng, S. Kong and S. Liu, Structure and dielectric properties of novel low temperature co-fired $Bi_2O_3$-$RE_2O_3$-$MoO_3$ (RE= Pr, Nd, Sm, and Yb) based microwave ceramics, *Ceram. Int.* **43**, 2017, 4570–4575.

**[38]** Y. Wang, K. Miao, W. Wang and Y. Qin, Fabrication of lanthanum doped $BaTiO_3$ fine-grained ceramics with a high dielectric constant and temperature-stable dielectric properties using hydro-phase method at

atmospheric pressure, *J. Eur. Ceram. Soc.* **37**, 2017, 2385–2390.

**[39]** Z. Xu, H. Qiang, Y. Chen and Z. Chen, Microstructure and enhanced dielectric properties of yttrium and zirconium co-doped $CaCu_3Ti_4O_{12}$ ceramics, *Mater. Chem. ~~Physics~~Phys.* **191**, 2017, 1–5.

**[40]** W. Holand and G.H. Beall, Glass Ceramic Technology, 2012, John Wiley & Sons, ~~ISBN: 978-0-470-48787-7~~(ISBN: 978-0-470-48787-7).

**[41]** M.D. Rigterink, Microscopic and X-ray investigation of some steatite bodies, *J. Am. Ceram. Soc.* **30**, 1947, 214–218.

**[42]** W.L. Brown, N. Moromoto and J.W. Smith, A structural explanation of the polymorphism and transition of $MgSiO_3$, *~~J.Geol.~~J. Geol.* **69**, 1961, 609–616.

**[43]** J.R. Smyth, Experimental ~~Study~~study on the ~~Polymorphism~~polymorphism of ~~Enstatite~~enstatite, *~~American Mineralogist~~Am. Mineral.* **59**, 1974, 345–352.

**[44]** M. Wesolowski, Thermal ~~Decomposition~~decomposition of ~~Talc: Review~~talc: review, *~~Thermoch.~~Thermochim. Acta* **78**, 1984, 395–421.

**[45]** A. Terzić, L. Pezo, Lj Andrić and M. Arsenović, Effects of mechanical activation on the parameters of talc quality for ceramics production - Chemometric approach, *Compos. B: Eng.* **79**, 2015, 660–666.

**[46]** A. Terzić, L. Pezo, N. Mijatović, J. Stojanović, M. Kragović, Lj Miličić and Lj Andrić, *~~„The~~The* effect of alternations in mineral additives (zeolite, bentonite, fly ash) on physico-chemical behavior of Portland cement based ~~binders“~~binders, *Constr. ~~Build.~~ Build. . Mater.* **180**, 2018, 199–210.

**[47]** A. Wiewiora, S. Sanchez-Soto, M. Avilos, A. Justo, L. Perez-Maqueda, J. Perez-Rodriguez and P. Bylina, Talc from Puebla de Lillo Spain I - XRD study, *Appl. Clay Sci.* **12**, 1997, 233–245.

**[48]** X. Kuang, X. Jing and Z. Tang, Dielectric loss spectrum of ceramic $MgTiO_3$ investigated by AC impedance and microwave resonator measurements, *J. Am. Ceram. Soc.* **89**, 2006, 241–246.

## Queries and Answers

**Query:**

Please confirm that given names and surnames have been identified correctly and are presented in the desired order, and please carefully verify the spelling of all authors.

**Answer:** The given names and surnames are correct. The spelling is correct. Also the order of the authors is correct.

**Query:**

Your article is registered as a regular item and is being processed for inclusion in a regular issue of the journal. If this is NOT correct and your article belongs to a Special Issue/Collection please contact k.mottram@elsevier.com immediately prior to returning your corrections.

**Answer:** Yes, the article is a regular item and it should be included in a regular issue of the journal.

**Query:**

Please validate the layout of Table 3.

**Answer:** The layout for the Table 3 is correct.

**Query:**

Please type the full funder name and country, plus grant IDs in the text, if available. Correctly acknowledging the primary funders and grant IDs of your research is important to ensure compliance with funder policies. Have we correctly interpreted the following funding source(s) you cited in your article: “Serbian Ministry of Education, Science and Technological Development”, “Serbia”?

**Answer:** The corrected text for the Acknowledgments should be as listed here: **This investigation was supported by the Ministry of Education, Science and Technological Development of the Republic of Serbia. The research was conducted under the following projects: ON 172057 (Directed synthesis, structure and properties of multifunctional materials) and III 45008 ( Development and application of multifunctional materials based on domestic raw materials by modernization of traditional technologies). The authors would like to express their**

**gratitude to Dr. Smilja Marković, Institute of Technical Sciences of SASA, Belgrade, Serbia, for providing help with the thermal analysis.**